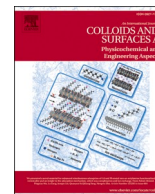Contents lists available at ScienceDirect

Colloids and Surfaces A: Physicochemical and Engineering Aspects

journal homepage: www.elsevier.com/locate/colsurfa

Nature-inspired trapped air cushion surfaces for environmentally sustainable antibiofouling

Joe M. Rawlinson [a], Harrison J. Cox [a], Grant Hopkins [b], Patrick Cahill [b], Jas Pal S. Badyal [a],*

[a] Department of Chemistry, Science Laboratories, Durham University, Durham DH1 3LE, England, UK
[b] Cawthron Institute, 98 Halifax Street East, Nelson, New Zealand

HIGHLIGHTS

- Bioinspiration from mallard duck feathers and the diving bell spider.
- Fabrication of trapped surface air layers.
- Long lasting and environmentally sustainable antibiofouling.

GRAPHICAL ABSTRACT
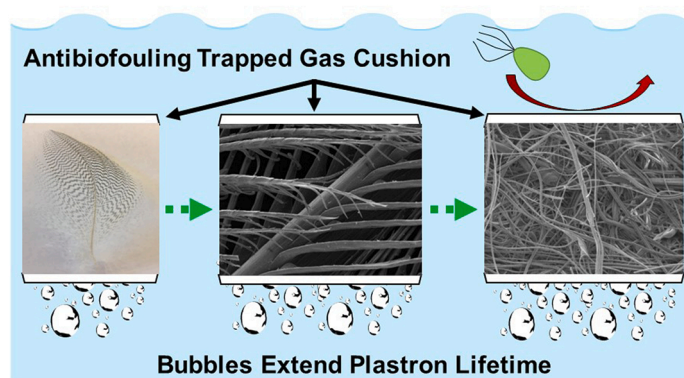
ARTICLE INFO

ABSTRACT

Feathers of seabirds and waterfowl (for example the mallard duck (*Anas platyrhynchos*)) consist of hierarchical fibrillar structures encapsulated with hydrophobic preen oil. These characteristics afford waterproofing through the entrapment of air pockets, enabling swimming and diving for such bird species. This liquid repellency mechanism for bird feathers is mimicked by surface hydrophobisation of fibrous nonwoven polypropylene textiles to create large volumes of trapped air at the solid–liquid interface (plastron). Higher static water contact angle values correlate to a greater resistance towards water ingress (akin to the behaviour of mallard feathers). In order to extend the trapped gas layer lifetimes, the transportation of air from the water surface to a submerged air bubble by the diving bell spider (*Argyroneta aquatica*) for respiration is mimicked via short duration (< 1 s) solar-powered air bubble bursts once every 2 h. This combination of ornithological and arachnological inspired approaches yields stable trapped gas layers at the solid–liquid interface which are shown to inhibit biofouling in real-world outdoor wet environments.

* Corresponding author.
  E-mail address: j.p.badyal@durham.ac.uk (J.P.S. Badyal).

1. Introduction

Natural world species ranging from waterfowl to aquatic spiders have evolved unique approaches for sustaining underwater entrapped air layers over long periods of time to facilitate diving into water [1,2]. For instance, mallard ducks (*Anas platyrhynchos*) spend a significant proportion of their time floating on water. Through the formation of an entrapped air layer, their fibrous feather structure exhibits remarkable water repellency and high resistance towards water penetration [3–6]. This trapped gas layer provides thermal insulation against heat loss to the surroundings which would otherwise cool the bird and require a greater production of metabolic heat to maintain its body temperature [7,8]. Any unintended water ingress into duck feathers can culminate in both direct [9,10] and indirect [10,11] causes of premature death. Water droplets resting on duck feathers are considered to be in the Cassie–Baxter state—in which trapped air pockets (plastron) minimise wetting with the rough solid surface culminating in super-hydrophobicity [12,13]. This roughness is attributed to the hierarchical structure of mallard feathers comprising multiple length scales of fibres (rachis, barbs, barbules, and hooklets) [14], Fig. 1. The central shaft (rachis) provides structural support for the feather. Fused to the rachis are a series of barbs, to which are attached smaller features known as barbules. These barbules occupy most of the area fraction of the feather, and themselves are covered with an array of even smaller protrusions called hooklets—which enable attachment to neighbouring barbules and barbs to form a continuous micro-fibrous structure [15]. The length, diameter, and spacing of feather barbs and barbules govern water repellency, and are optimal through natural evolution for different bird species according to their local habitats/behaviours [1,5,16]. This concerted hierarchical surface roughness in combination with the hydrophobicity of the preen oil (complex mixture formed mainly of lipids [17,18]) coating gives rise to the high liquid repellency observed for mallard duck feathers [19].

A variety of fabrication techniques have previously been employed to replicate the water repellency properties of bird feathers (such as waterfowl (*Anatidae*)), including: electrospinning [20,21], wet

Fig. 1. (a) Photograph of a mallard breast feather; (b) hierarchical length scale structure of mallard breast feathers where angles are measured to be α = 41.6 ± 4.9°, β = 43.0 ± 3.2°, and γ = 39.2 ± 5.9° respectively; and (c–e) scanning electron microscopy (SEM) images of mallard feather. See Supplementary Material Fig. S1 for further details about orientation of barbules and hooklets underneath.
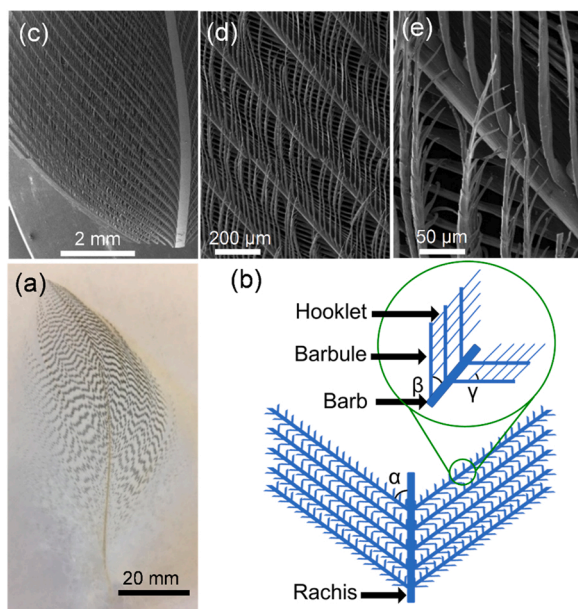
polysiloxane-functionalisation of cotton and polyester fabrics [22], 3D-printing [23], laser cutting [24], and surface modification of polymers with photonic crystals [25]. However, these investigations solely focused on the materials water repellency or the pressure stability of trapped air pockets within their structure, rather than their ability to retain air at the solid–liquid interface over extended periods of time in order to prevent biofouling.

On the other hand, gas entrapment materials have utilised large pore fractions to maximise gas volume capture (e.g. nanowire architectures [33], textiles [26–29], and membranes [30]) [31–33]. Such gas layers trapped at solid–liquid interfaces are effective at deterring the attachment of bacteria [34,35] and reducing drag [36]. However, they suffer from being operational for only limited time periods due to the gas layers dissipating into the surrounding bulk fluid—culminating in their eventual collapse [31,37,38]. Such plastron depletion remains one of the biggest challenges for the practical applicability of superhydrophobic surfaces submerged underwater for long periods. One potential solution is to employ micro/nano-structured surfaces which can sustain the vapour phase of water and/or trapped gases within the surface roughness [39,40]. Other attempts to address this drawback have included: the heating of water-immersed thermally conductive superhydrophobic materials [41,42], self-regulated electrolysis to produce hydrogen bubbles at the solid–liquid interface [43], air injection directly onto microstructured water repellent solid surfaces [44,45], applying steady gas pressure behind porous superhydrophobic surfaces to prevent water ingress [46,47], and combining hydrophobic elements with hydrophilic tips in conjunction with gas recharge systems [48,49]. These proposed solutions require continuous electrical power supply, complex construction, or do not provide complete gas layer area coverage—leading to limited antifouling and drag reduction properties [50].

Another natural living species which relies upon trapped air layers in aquatic environments is the diving bell spider (*Argyroneta aquatica*) [51]. This spider spends almost its entire life underwater and breathes air trapped either in a large bubble (anchored to aquatic foliage by a hydrophilic silk web), or located on its abdomen—which acts as a physical gill [1]. To maintain a steady concentration of oxygen in the bubble for respiration, the submerged spider frequently travels up to the water surface to capture air onto its hairy aerophilic abdomen, and then transports this air layer down to its deep-water reservoir [52,53]. This periodic regeneration of the web encased submerged air bubble allows the spider to respire underwater indefinitely [52]. Superhydrophilic (aerophobic) meshes, inspired by the behaviour of the diving bell spider, have been used to trap air volumes underwater [54]. However, this approach relies on water being tightly bound within the structure of the mesh and therefore air is not trapped within the porous mesh structure or at the solid–liquid interface.

Gas bubble capture and transport through structures has been reported using micro-drilled superhydrophobic surfaces (laser ablated PTFE and PDMS), this approach is limited because it does not lead to the formation of a three-dimensional air cushion within the bulk material, and the longevity of air layers entrapped at the solid–liquid interface has not been explored [55–58]. Previous attempts to utilise air bubbles to recharge trapped air layers have solely used floating (not submerged) substrates, these have been shown to be only effective over relatively short periods (1 h) and at negligible hydrostatic pressures, with the gas bubbles effectively lifting the structure surface out of the water (i.e. the substrate briefly losing contact with the bulk liquid), and therefore offering only limited applicability to real-world totally submerged substrate scenarios [30].

In this article, the gas trapping properties of mallard feathers are mimicked using superhydrophobic surface functionalisation of nonwoven polypropylene textiles to create a micro-fibrous liquid repellent porous substrate. This structure is combined with the underwater gas volume replenishment behaviour of the diving bell spider by using a solar-powered pulsed bubble generator to sustain a trapped gas layer at the solid–liquid interface over prolonged periods. Immersion of these

trapped air cushion layers into outdoor pond water significantly extends the lifetime of antibiofouling performance.

2. Materials and methods

2.1. Materials

Mallard breast feathers acquired from the bird (Cookshill Fly Tying Co.) were used unwashed in order to preserve their natural state and avoid structural damage. To artificially replicate the fibrillar length-scale structure of the feathers, two fine meltblown nonwoven polypropylene textiles ((20 g m^{-2} grade, Product No. M020A1WMS, Don & Low Ltd) and (35 g m^{-2} grade, Product No. M035A1WOO, Don & Low Ltd)) of different weights were used with fibre diameters (3.4 ± 1.9 µm and 4.1 ± 2.3 µm for the 20 g m^{-2} grade and 35 g m^{-2} grade textiles respectively) comparable to mallard feather barbule diameters (8.4 ± 1.5 µm). Nonwoven textiles were cut into approximately 35 mm × 70 mm pieces and cleaned by placing into a 50/50 v/v solvent mixture of cyclohexane (+99.5%, Fisher Scientific UK Ltd) and propan-2-ol (+99.5%, Fisher Scientific UK Ltd) for 3 h. The samples were then dried in air at ambient temperature for at least 2 h.

Plasmachemical surface functionalisation utilised carbon tetrafluoride feed gas (CF$_4$, +99.7% purity, Air Products and Chemicals Inc) and was conducted in a cylindrical glass reactor (5 cm internal diameter, 470 cm^3 volume, base pressure lower than 9×10^{-3} mbar, and a leak rate better than 6×10^{-10} mol s^{-1}) enclosed in a Faraday cage [59,60]. The reactor was connected to a 30 L min^{-1} two-stage rotary pump (model E2M2, Edwards Ltd) via a liquid nitrogen cold trap. An inductor–capacitor impedance matching network was used to minimise the standing-wave ratio for power transmission from a 13.56 MHz radio frequency (RF) generator (model ACG-3, ENI Technology Inc) to a copper coil (10 turns, spanning 8 cm) wound externally around the glass chamber. The reactor was scrubbed with detergent, rinsed with propan-2-ol, and oven-dried at 200 °C. A continuous wave air plasma was then ignited at 50 W power and 0.2 mbar pressure for at least 30 min in order to remove any remaining contaminants, followed by ignition of a continuous wave CF$_4$ gas plasma at 30 W power and 0.2 mbar pressure for 10 min to condition the glass reactor walls. Non-woven polypropylene textiles were placed against the interior chamber wall avoiding any overlap. The system was evacuated to base pressure and purged with CF$_4$ gas at a pressure of 0.2 mbar for 15 min. The CF$_4$ electrical discharge was then reignited at various RF powers and allowed to run for 2 min. Upon termination of the CF$_4$ plasma exposure, the RF power generator was switched off, and CF$_4$ gas allowed to purge the chamber for a further 5 min. Finally, the system was evacuated to base pressure and vented to atmosphere. For static water contact angle and hydrostatic breakthrough measurements, nonwoven polypropylene textiles were exposed to CF$_4$ plasma on one face (2 min); whilst for solid–liquid interface trapped gas layer longevity and bubble experiments, both sides were sequentially CF$_4$ plasma treated (2 min on each side).

2.2. Surface characterisation

2.2.1. Scanning electron microscopy

Cut pieces of mallard feather and nonwoven polypropylene textiles were mounted onto carbon disks supported on aluminium stubs (part no. S111, TAAB Laboratories Equipment Ltd) and then coated with a thin gold layer (5 −10 nm, Polaron E500 SEM Coating Unit, Quorum Technologies Ltd). Surface topography images were acquired using a scanning electron microscope (model Vega 3LMU, Tescan Orsay Holdings a. s.) operating in the secondary electron detection mode, in conjunction with an 8 kV accelerating voltage and a working distance of 8 − 11 mm. For high resolution images, nonwoven textiles were first coated using a carbon coater (model 108carbon/A, Cressington Scientific Instruments Ltd) and then electron micrographs acquired using a scanning electron

microscope (Karl Zeiss Sigma 300 VP FE-SEM, Carl Zeiss Ltd).

2.2.2. Porosity

Optical microscopy of nonwoven polypropylene textiles was performed under fixed lighting conditions using a digital microscope (model MicroDirect® 1080p HD, Celestron LLC). Thirty images of different cross-sectional areas of textile samples were taken in conjunction with a calibration ruler to determine each magnification. Images were then analysed using the ImageJ software. Using the thickness measurements and known textile weight, the porosity was then calculated using the densities of polypropylene and air (905 kg m^{-3} and 1.2 kg m^{-3} respectively) [61,62].

2.2.3. Surface area

Samples were dried overnight in a vacuum oven at room temperature. A surface area analyser (model Gemini VII, Micromeritics Instrument Corporation) was used for Brunauer–Emmett–Teller (BET) to determine surface area values. Nitrogen adsorption was measured at liquid nitrogen temperature to provide adsorption–desorption isotherms, and the surface area calculated according to the BET method.

2.2.4. X-ray photoelectron spectroscopy

X-ray photoelectron spectroscopy (XPS) was carried out using an electron spectrometer (ESCALAB II, VG Scientific Ltd) fitted with an unmonochromatized Mg Kα X-ray source (1253.6 eV) and a concentric hemispherical analyser. Photoemitted electrons were collected at a take-off angle of 20 ° from the substrate normal with electron detection in the constant analyser energy mode (CAE mode pass energy = 20 eV). A linear background was subtracted from core-level spectra and then fitted using Gaussian peak shapes with a constant full-width-at-half-maximum [63]. Experimentally determined instrument sensitivity (multiplication) factors were C(1 s): F(1 s) = 1.00: 0.25.

2.2.5. Surface wetting

Static water contact angles were measured using 7.0 µL high purity water droplets (BS 3978 grade 1) and a video contact angle goniometer (VCA 2500 XE, AST Products Ltd). Smaller size droplets could not be dispensed from the water syringe needle tip due to the highly liquid repellent nature of the CF$_4$ plasma functionalised nonwoven polypropylene surfaces. Advancing and receding (dynamic) contact angle values were measured by decreasing the dispensed 7.0 µL water droplet by 3.0 µL at a rate of 0.1 µL s^{-1} and then subsequently increasing the droplet volume by 3.0 µL at a rate of 0.1 µL s^{-1} respectively [64]. Droplet images were analysed using ImageJ software in conjunction with the Dropsnake plugin [65]. Static water contact angle values were calculated from measurements taken at three random points on each of three separate samples, and the propagated standard deviation used for the error value.

Sliding angle measurements were undertaken at 20 °C using a V-block adjustable angle gauge (model Adjustable Angle Gauge/Tilting Vee Blocks Small, Arc Euro Trade Ltd). This entailed placing samples onto the stage at an initial angle of 0° and dispensing a 50 µL droplet onto the surface. The inclination of the stage was then increased by 1° every 15 s until movement of the water droplet was observed [66].

Captive bubble contact angle analysis was carried out on porous materials with the video capture system in combination with a captive bubble attachment dispensing approximately 1 µL air bubbles (VCA captive bubble accessory, AST Products Inc).

2.3. Hydrostatic breakthrough pressure

A nitrile rubber O-ring (23 mm outer diameter, RS Components Ltd) wrapped in PTFE tape (part no. 2ptfewater, Everbuild Building Products Ltd) was inserted into the central body of a dismantled brass connector (1-inch internal diameter, Cajon Co.). Nitrile rubber O-rings (25 mm outer diameter, RS Components Ltd) were located on either side of a

piece of 35 mm $\times$ 35 mm nonwoven polypropylene textile and inserted into the brass connector to create a watertight seal, Supplementary Material Fig. S2. The brass connector fitting containing the sample was attached to a 1 m long graduated glass tube (1-inch outer diameter and 23 mm internal diameter), Fig. 2. A burette was used to pour water into the top of the graduated tube at a flowrate of 30 cm^3 min^{-1}. In order to ensure a steady and even rise in hydrostatic pressure across the textile surface, care was taken to position the burette so that water flowed down the graduated tube walls and did not drip directly onto the textile. The meniscus height at which water first penetrated through the textile was taken for calculation of the hydrostatic breakthrough pressure [67, 68]. Hydrostatic breakthrough pressures were calculated from measurements taken for at least three separate samples, and the standard deviation used for the error value.

2.4. Solid–liquid interface trapped gas layer and bubbles

Trapped gas layer formation at the solid–liquid interface of porous materials (i.e., mallard feathers and textiles) submerged in tap water was observed using a glass chamber, Fig. 2 and Supplementary Material Fig. S4. The bottom of the glass chamber was fitted with a 4 mm glass tube inlet which could be used to introduce gas bubbles to the system. Two outer aramid fibre–nitrile blend rubber composite gaskets (27 mm internal diameter, 59 mm external diameter, part no. OFM0030001500002069A, Klingersil C4400, Klinger Ltd) were used to secure each square 35 mm $\times$ 35 mm test piece onto a glass support ring such that the sample completely covered the outer gasket and support ring holes, Supplementary Material Fig. S4. Four strips of adhesive tape (part no. SLT1629146, Henkel Ltd) were used to press the two outer gasket seals tightly against the sample piece and glass support ring. The cylindrical glass chamber was filled with tap water to 10 cm above the internal glass support lip, and then the pre-assembled gasket–porous material–glass support ring–gasket assembly was lowered into the glass chamber to rest on the internal glass support lip to create a trapped air layer at a hydrostatic pressure of 0.93 kPa (9.5 cm of water above the

Fig. 2. Apparatus for: (a) hydrostatic breakthrough test; and (b) solid–liquid interface trapped gas layer bubble chamber. For sample holder assembly details see Supplementary Material Fig. S2, Fig. S3, and Fig. S4.

test sample upper surface), Fig. 2. The trapped gas layer located at the upper solid–liquid interface was visible to the naked eye and gave the test sample surface a shimmering silvery appearance due to the total internal reflection of light at the liquid–gas interface characteristic of the superhydrophobic state [69].

In order to monitor the trapped air layer longevity at the sample surface, the gas inlet of the glass chamber was sealed off using plastic wrapping film (product no. PM-999, Amcor plc) prior to filling the system with tap water, Fig. 2. The glass chamber was then filled with water up to 10 cm above the glass support lip and the pre-assembled gasket–porous material–glass support ring–gasket assembly was lowered into the glass chamber to rest on the internal glass support lip, Fig. 2 and Supplementary Material Fig. S4. Test samples placed into cylindrical glass chambers were inspected (photographed) on a daily basis until the shiny silver surface (gas layer) disappeared. The upper water level was topped up regularly to avoid evaporation effects by pouring water down the chamber side walls to maintain a steady and even hydrostatic pressure across the upper textile surface. A light source (model no. G1330, Gritin Co.) was placed 10 cm behind each glass chamber to improve visibility of the shiny silver gas layer at the upper textile surface. Trapped air layer longevity values were calculated as the average from at least three separate samples, and the standard deviation used for the error value.

For trapped gas layer critical surface bubble diameter measurements, nitrogen gas bubbles were introduced at a flowrate of 30 cm^3 min^{-1} through the 4 mm glass tube inlet into the bottom of the glass chamber regulated with a fine control needle valve (model MN, CT Platon Ltd) and monitored using a gas flowrate meter (model Flostat NG, CT Platon Ltd), Fig. 2. Diameters of at least 15 gas bubbles visible in the upper surface trapped gas layer of each submerged test sample were measured from videos filmed using a 12-megapixel camera (model A1688, Apple Inc). Critical bubble diameter values (maximum bubble size before surface detachment) were calculated from the average diameter of three separate samples, and the propagated standard deviation used for the error value.

For solid–liquid interface trapped gas cushion longevity experiments with additional gas injection for recharging, air bubbles lasting less than 1 s (total volume 1.9 $\pm$ 0.8 mL) were injected through the gas inlet once every 2 h using a solar-powered air pump (model no. BSV-AP002, Shenzhen SanShang Technology Co.; this was modified to generate < 1 s short bursts of bubbles), Fig. 2. Continuous streams of air bubbles could not be used for recharging in the glass chamber as the pressure build-up below the porous materials led to premature gas cushion collapse or lifting of the gasket–porous material–glass support ring–gasket assembly after a few hours. The trapped gas cushion was considered to have collapsed either when the topmost surface lost its shiny silvery appearance or when the sample bulged upwards due to the blockage of gas transport through the porous material as a consequence of the air layer located on the bottom of the sample having at least partially collapsed (liquid ingress) [55,70]. Trapped air cushion longevity values were calculated as the average from at least three separate samples, and the standard deviation used for the error value.

2.5. Biofouling

Antibiofouling capabilities of the 20 g m^{-2} grade nonwoven polypropylene textile were assessed by placement into a large plastic tank (volume = 115 L, temperature range: 9–13 °C), fitted with two metal rods from which to hang samples and filled with water from a nearby pond, Supplementary Material Fig. S5. 15 mL of water-soluble fertiliser (Miracle-Gro All Purpose Plant Food, Scotts Miracle-Gro Co.) was added to the biofouling tank water every other week in order to enhance the growth rate of natural biofouling species contained in pondwater [71]. The water temperature at a depth of ~15 cm was also monitored.

In a typical experiment, samples were fixed in mounts (part no. PM-9425, Matin International Co.) and then firmly attached to the top of a
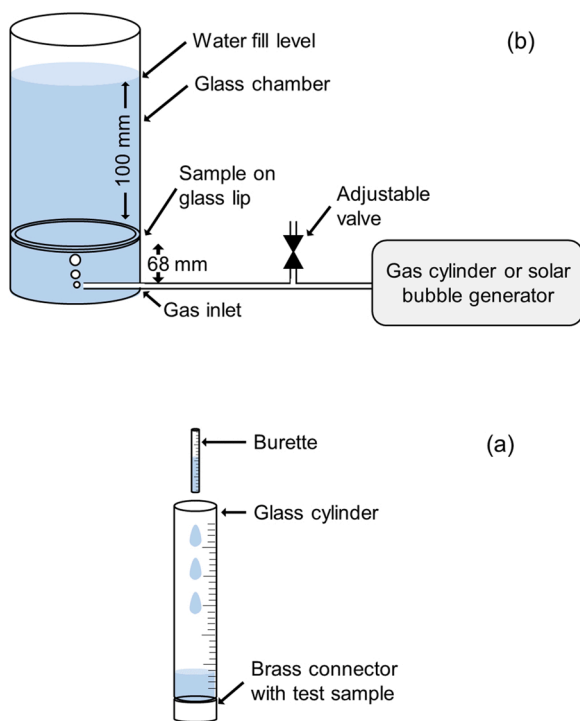
modified plastic box (model no. HPL822B, Locknlock Co.) to form a sample–mount–box assembly. A continuous bubble stream was used for biofouling experiments to maximise the trapped gas cushion recharging of porous materials as excess air bubbles could be released through holes in the sample–mount–box assembly. The box had four 30 mm × 40 mm holes cut in the upper face to allow water, fouling material and/or air bubbles to easily reach the lower test sample surfaces, Supplementary Material Fig. S5. Samples were photographed using a 12-megapixel camera (model A1688, Apple Inc) and then the sample–mount–box assembly was placed into the tank at a depth of ~15 cm for 7 days. Samples were immersed in either stationary pond water or placed above a continuous stream of air bubbles (~1200 cm^3 min^{-1}) supplied by the modified solar air pump through plastic gas tubing (internal diameter = 4 mm) placed 7 cm below the centre of four samples mounted in the sample–mount–box assembly. After removal from the tank, the sample–mount sections were detached from the plastic box and gently dipped two times in fresh tap water to remove any unadhered fouling material from the surface and then photographed in fixed lighting conditions.

Colour measurements can be used to provide a rapid quantitative measure of biofouling accumulation with a larger colour change indicative of higher levels of surface fouling [72,73]. At least three colour measurements of each nonwoven polypropylene sample were taken both before and after pond water immersion using a colourimeter (model PCE-CSM 4, PCE Instruments UK Ltd) under fixed lighting conditions and with a constant backing colour. The colour change of samples during pond water immersion was then calculated in the CIELAB colour space using Eq. (1). Where $L*$ is the lightness of the colour, $a*$ is the position between red and green, and $b*$ is the position between blue and yellow [74].

$$\Delta E = \sqrt{\Delta L^{*2} + \Delta a^{*2} + \Delta b^{*2}} \qquad (1)$$

3. Results

3.1. Surface characterisation

3.1.1. Scanning electron microscopy

Scanning electron microscopy (SEM) of mallard feathers revealed a hierarchical structure spanning different length scale features—rachis, barbs, barbules, and hooklets with diameters of 284.5 ± 10.4 μm, 34.9 ± 2.2 μm, 8.4 ± 1.5 μm, and 2.6 ± 0.4 μm respectively, Fig. 1. These feature sizes are comparable in scale to previous studies where the mallard feather barb and barbule diameters were measured to be 46 μm and 4.4 μm respectively [75,76]. The barbules run transverse over those of the adjoining barb (directional overlapping), with hooklets oriented towards underlying barbs for attachment. Nanotextured axial grooves are visible on the barb and barbule surfaces, Supplementary Material Fig. S6. The angle between the feather barbs and the central rachis was measured to be 41.6 ± 4.9°, whilst the angle between the barbules and barbs was 43.0 ± 3.2°. Examination of the hooklets lying in the plane of the SEM image estimated the angle between hooklets and barbules to be 39.2 ± 5.9°. Overall, these features combine to form a continuous micro-fibrous surface structure.

Both types of nonwoven polypropylene textile surface (20 g m^{-2} and 35 g m^{-2}) comprise a continuous random fibrous structure, Fig. 3 and Supplementary Material Fig. S7. Electron microscopy showed the fibre diameters to be in the micron range, which is on a comparable length scale to the mallard feather barbule and hooklet features, Fig. 1. The fibre surface topography remained largely unchanged following 30 W CF$_4$ plasma exposure—which can be attributed to the mild rather than more reactive electrical discharge conditions employed [77], Supplementary Material Fig. S6. No noticeable structural differences were evident between CF$_4$ plasma treatment of nonwoven polypropylene on one side versus both sides, Supplementary Material Fig. S8.
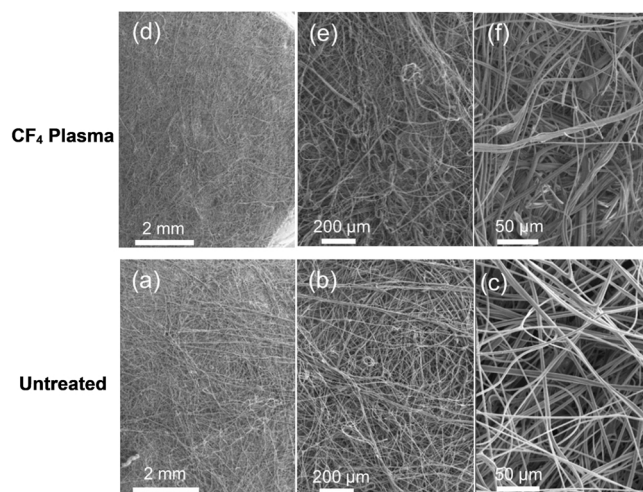
Fig. 3. Scanning electron microscopy (SEM) images of nonwoven polypropylene (20 g m^{-2}): (a–c) untreated; and (d–f) CF$_4$ plasma treated on both sides (30 W). High resolution images provided in Supplementary Material Fig. S6.

3.1.2. Porosity

Optical microscopy reveals thickness measurements of 0.25 ± 0.03 mm and 0.32 ± 0.03 mm for the 20 g m^{-2} and 35 g m^{-2} nonwoven polypropylene textiles respectively, Supplementary Material Fig. S9. The calculated porosity of the lighter 20 g m^{-2} material (0.91 ± 0.01) is therefore greater than for the 35 g m^{-2} textile (0.88 ± 0.01). This relationship between textile weight and porosity is typical for nonwoven materials produced by the same manufacturing method [78, 79].

3.1.3. Surface Area

The BET specific surface areas of the 20 g m^{-2} and 35 g m^{-2} nonwoven polypropylene textiles were measured to be 1.25 ± 0.02 m^2 g^{-1} and 1.26 ± 0.02 m^2 g^{-1} respectively. In addition, similar adsorption/desorption isotherms were acquired for the two materials. These isotherms indicate that the textiles consist of a macroporous structure made up of smooth nonporous fibres [80], Supplementary Material Fig. S10.

3.1.4. X-Ray Photoelectron Spectroscopy

XPS analysis of the untreated nonwoven polypropylene detected the presence of only carbon (hydrogen is not detectable by XPS), Supplementary Material Fig. S11. An elemental F:C ratio of 1.29:1.00 was measured following CF$_4$ plasma treatment, which is consistent with previously reported F:C ratio values for CF$_4$ plasma treated polypropylene surfaces [81,82].

3.1.5. Surface Wetting

Mallard feathers exhibited a high static water contact value (154.8 ± 5.7°) due to a multiple length scale hierarchical structure and hydrophobic preen oil[14], Fig. 3.

The micro-fibrous topography and hydrophobicity of nonwoven polypropylene (20 g m^{-2} grade) also provided a high static water contact angle value (148.3 ± 4.6°). The level of hydrophobicity increased with CF$_4$ plasma treatment power reaching a maximum value of 160.6 ± 4.6° for 30 W electrical discharge power, Fig. 4. Higher power CF$_4$ plasma treatments (40 W and 50 W) yielded slightly lower water contact angle values, which is most likely due to surface damage of the fibrillar structure by more energetic electrical discharge species [83,84]. An increase in hydrophobicity following optimal CF$_4$ plasma treatment (30 W) is accompanied by a decrease in water contact angle hysteresis (from 15.0 ± 6.1° for untreated textile to 3.1 ± 0.9° for functionalised
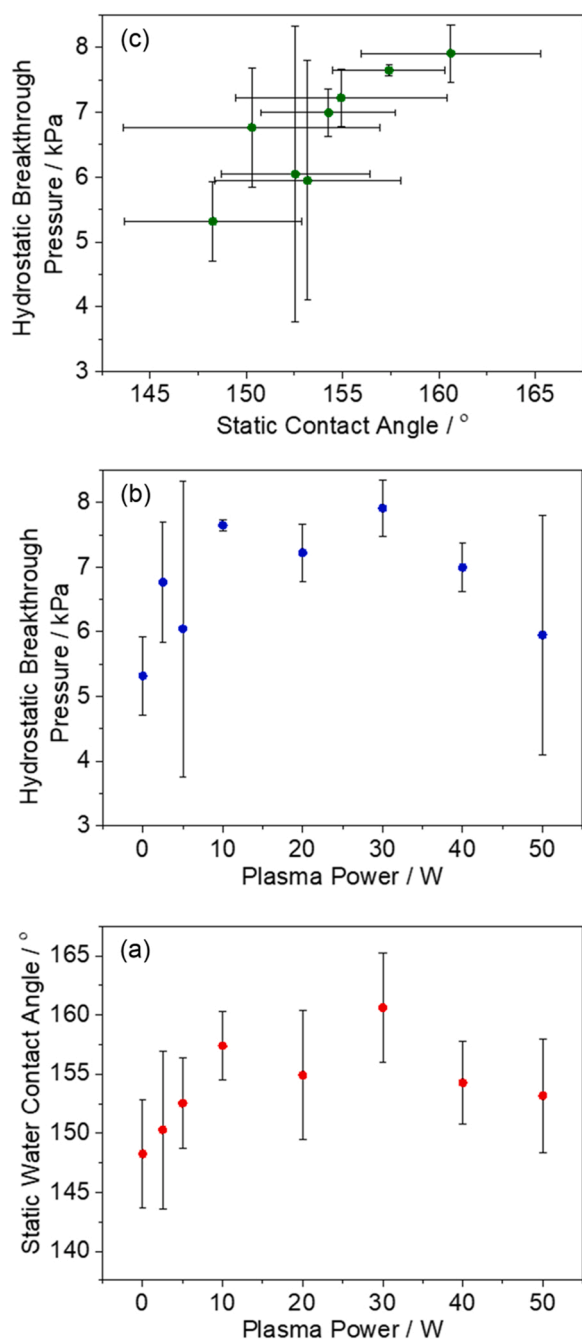
Fig. 4. CF$_4$ plasma treatment of nonwoven polypropylene (20 g m^{-2}) as a function of electrical discharge power (0–50 W, treated on side facing water): (a) static water contact angle values; (b) hydrostatic breakthrough pressure; and (c) hydrostatic breakthrough pressure plotted against respective static water contact angle values.

textile) and sliding angle (from $14.8 \pm 2.7°$ for untreated textile to $2.9 \pm 0.9°$ for functionalised textile) values.

3.2. Hydrostatic Breakthrough Pressure

Untreated 20 g m^{-2} grade nonwoven polypropylene textile displayed a hydrostatic breakthrough pressure of 5.3 ± 0.6 kPa, Fig. 4. Breakthrough pressure increased following CF$_4$ plasma treatment for powers ranging between 2.5 and 50 W, reaching over 25% enhancement at 30 W electrical discharge power (maximum value of 7.9 ± 0.4 kPa). At higher CF$_4$ plasma powers (40 and 50 W), the textile hydrostatic

breakthrough pressure dropped—probably due to high power energetic plasma species damaging the polymer surface [83,84]. A good correlation is found between hydrostatic breakthrough pressure and measured static water contact angle values, Fig. 4.
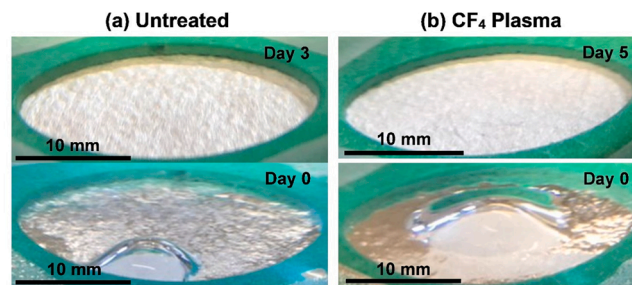
3.3. Solid–liquid Interface Trapped Gas Layer and Bubbles

The optimal CF$_4$ plasma power treated nonwoven polypropylene textile (20 g m^{-2}, 30 W, corresponding to the greatest combined static water contact angle ($160.6 \pm 4.6°$) and hydrostatic breakthrough pressure (7.9 ± 0.4 kPa)) was tested further for entrapped gas layer stability under water immersion, Fig. 2, Fig. 4, and Fig. 5. A shimmering shiny silver appearance was taken as diagnostic of gas entrapment at the immersed solid–liquid interface [85], Fig. 5. The enhancement of silvery brightness for CF$_4$ plasma treated nonwoven polypropylene textile indicated the formation of a thicker trapped gas layer, Fig. 5 [44].

When no bubbles were injected into the glass chamber, gradual deflation of the upper solid–liquid interface gas layers was observed over time. This led to eventual disappearance of the shiny silver shimmer, which is consistent with complete loss of the air layer–water interface (due to water ingress). CF$_4$ plasma treatment of nonwoven polypropylene textile extended the trapped gas layer longevity from 2.5 ± 0.9 days (untreated) to 4.8 ± 1.1 days, Fig. 5, and Table 1.

Similar static contact angle and critical surface bubble diameter values were measured for the 20 g m^{-2} grade and 35 g m^{-2} grade nonwoven polypropylene substrates, both when untreated and following CF$_4$ plasma functionalisation—this is consistent with both of these measurements being dominated by surface topography and chemistry of the substrate, Table 1. Whereas, the higher weight nonwoven polypropylene (35 g m^{-2} grade) has significantly shorter trapped gas layer lifetimes for both untreated (1.3 ± 0.5 days) and CF$_4$ plasma functionalised samples (2.7 ± 0.5 days) compared to the 20 g m^{-2} grade counterparts (2.5 ± 0.9 days and 4.8 ± 1.1 days respectively)—possibly due to the lower bulk porosity of this material (0.88 ± 0.01 for 35 g m^{-2} grade vs 0.91 ± 0.01 for 20 g m^{-2} grade). This confirms the role of the bulk air cushion rather than just an outer substrate surface solid–liquid interface effect.

A stream of gas bubbles introduced from below the porous materials instantaneously coalesce with entrapped air layers, thereby increasing the volume of gas contained within the textiles [86]. This is confirmed by captive bubble analysis, where the gas bubbles instantly transport into the submerged porous layer, Supplementary Material Video S1, Video S2, and Video S3. Buoyancy forces gas upwards causing accumulation on the upper surface and the formation of bubbles at the upper gas layer–liquid interface, which upon reaching a critical volume become unstable and detach into the bulk fluid rising due to buoyancy [56]. CF$_4$ plasma treatment of the nonwoven polypropylene textiles significantly increases the critical surface bubble diameters, Table 1 and

**Fig. 5.** Solid–liquid interface trapped gas layer longevity of nonwoven polypropylene (20 g m^{-2}) immersed in water using trapped gas layer bubble chamber (no additional bubbles): (a) untreated; and (b) CF$_4$ plasma treated (30 W, on both sides). Upon initial immersion the porous materials trap an air bubble on their upper surface, which forms without the injection of additional gas from below.

Table 1

Static contact angle value, trapped gas layer longevity (no additional bubbles), and surface bubble diameter formed during continuous bubble release (30 cm^3 min^{-1}) below samples of 20 g m^{-2} versus 35 g m^{-2} grade nonwoven polypropylene textiles before and after CF$_4$ plasma treatment (30 W, on both sides).

| Textile	Mass per Unit Area / g m^{-2}	Static Water Contact Angle / °	Trapped Gas Layer Longevity / days	Critical Surface Bubble Diameter / mm
Untreated	20	148.3 ± 4.6	2.5 ± 0.9	6.5 ± 1.8
	35	149.6 ± 3.1	1.3 ± 0.5	6.9 ± 0.7
CF$_4$ Plasma	20	160.6 ± 4.6	4.8 ± 1.1	13.0 ± 2.0
	35	159.4 ± 2.8	2.7 ± 0.5	13.7 ± 2.1
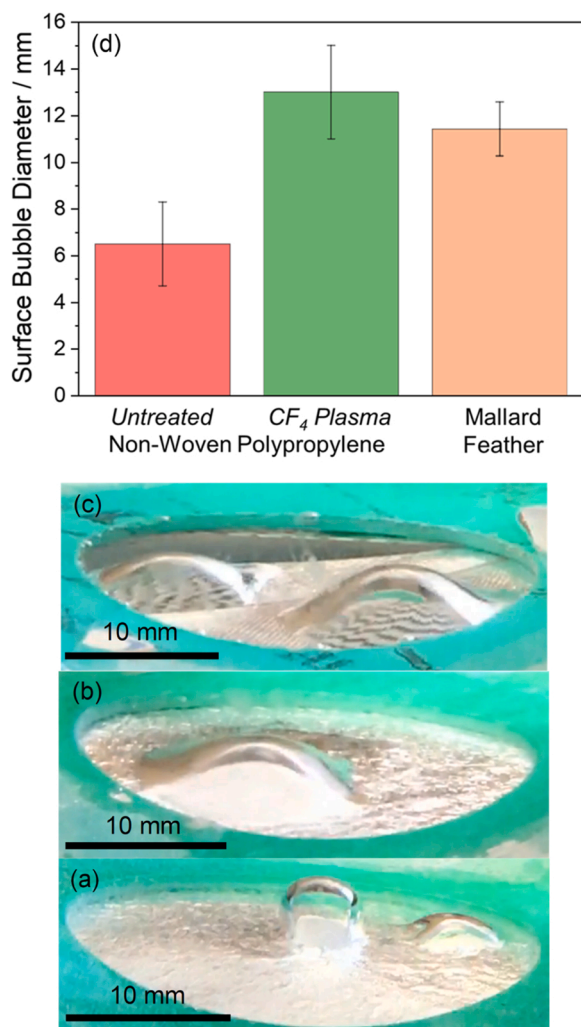
Fig. 6. Photographs of gas bubble formation on the water submerged sample upper surface in the trapped gas layer bubble chamber with a continuous stream of bubbles (nitrogen, 30 cm^3 min^{-1}) injected from below: (a) untreated nonwoven polypropylene (20 g m^{-2}) (Supplementary Material Video S4—small bubbles spreading around the surface); (b) CF$_4$ plasma treated nonwoven polypropylene (20 g m^{-2}, 30 W on both sides) (Supplementary Material Video S5—large gas bubble spreading around the surface); (c) untreated mallard feather (Supplementary Material Video S6—large bubble); and (d) comparison of nitrogen gas critical surface bubble diameters formed in the trapped gas layer at the solid–liquid interface (maximum value prior to detachment).

Fig. 6. This can be attributed to the increased gas layer thickness of the CF$_4$ plasma functionalised nonwoven polypropylene meaning fewer fibres (which act as pinning sites for the three-phase contact line)

protrude into the fluid [87]. The observed increase in surface bubble diameter demonstrates that the more hydrophobic and aerophilic CF$_4$ plasma functionalised nonwoven polypropylene can accommodate much larger volumes of gas (bubbles) before surface detachment compared to untreated nonwoven polypropylene textile [44]. Mallard feather samples display surface bubble diameters of 11.4 ± 1.2 mm—which are comparable in size to 30 W CF$_4$ plasma treated 20 g m^{-2} nonwoven polypropylene (bubble diameter of 13.0 ± 2.0 mm). In all cases, a continuous stream of bubbles injected below the substrate led to a stable gas layer at the upper facing solid–liquid interface. However, over prolonged periods the continuous release of bubbles into the glass chamber led to either premature gas cushion collapse (sample bulging) or lifting of the gasket–porous material–glass support ring–gasket assembly—this is likely due to the lack of a pressure release system below the sample.

Gas cushion longevity for the best performing material (CF$_4$ plasma functionalised 20 g m^{-2} nonwoven polypropylene) could be further improved through replenishment of the trapped gas layer at the upper solid–liquid interface by pulsing air bubbles (< 1 s bursts, total volume = 1.9 ± 0.8 mL) every 2 h from underneath the substrate. Continuous streams of air bubbles could not be used for recharging in trapped gas cushion longevity studies because the pressure build-up below the porous materials led to premature air cushion collapse. Using pulsed bubble release, the longevity increased from 2.0 ± 0.8 days to at least 29.0 ± 2.0 days for untreated versus CF$_4$ plasma functionalised nonwoven polypropylene respectively, Fig. 7. The longevity of solid–liquid interface trapped gas layers for untreated nonwoven polypropylene was not improved by using solar-powered pulsed air bubbles. This is possibly due to the associated pressure increases/fluctuations being sufficient to trigger liquid ingress (blockage) of the untreated textile's bottom surface leading to gas build-up which lifts the sample upwards, creating a visible bulge [88,89]. Therefore, a bulge indicates collapse of the trapped gas cushion encompassing the entire porous volume of the textile due to liquid penetration into the bottom surface causing wetting of the textile fibres on this face [55–57]. Whereas intermittent pulsing of air bubbles into the solid–liquid interface trapped gas layer of CF$_4$ plasma functionalised 20 g m^{-2} grade nonwoven polypropylene significantly extends gas cushion lifetimes with a thick and consistent plastron layer still present on flat (no gas build up below) samples after 29 days, Supplementary Material Fig. S12. This mimics the gas-replenishing behaviour of the diving bell spider. The extended period taken for the CF$_4$ plasma functionalised 20 g m^{-2} grade nonwoven polypropylene to bulge shows it can transport gas through its
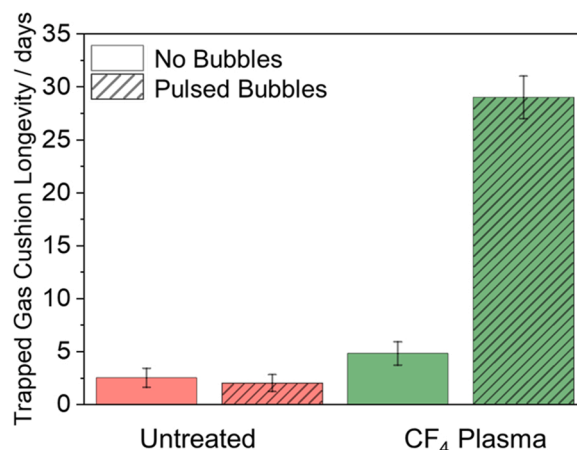
Fig. 7. Solid–liquid interface trapped gas cushion layer longevity in water for untreated and CF$_4$ plasma treated (30 W on both sides) nonwoven polypropylene (20 g m^{-2}) with no initial bubble injection and pulsed gas bubbles released every 2 h (< 1 s bursts, total volume = 1.9 ± 0.8 mL) to sustain the solid–liquid interface trapped gas layer.

porous structure more effectively under hydrostatic pressure than the untreated sample. However, even after sample bulging the functionalised 20 g m^{-2} grade nonwoven polypropylene samples maintained a shiny upper surface—attributable to much slower transport of gas through the porous structure as a consequence of deterioration of the trapped gas layer at the downwards facing textile surface [90,91].

3.4. Biofouling

Untreated nonwoven polypropylene was extensively fouled with green slime after 7 days of immersion in pond water under accelerated biofouling conditions, Fig. 8. The CF$_4$ plasma treated nonwoven polypropylene was significantly less fouled compared to the untreated material which correlates to increased trapped air layer longevity relative to the untreated material (2.5 ± 0.9 days and 4.8 ± 1.1 days for untreated and CF$_4$ plasma treated respectively in glass chamber apparatus). However, as the entrapped air layer dissipates, the surface does become fouled and will likely eventually become completely covered in organic material [31].

The continuous release of air bubbles below the untreated nonwoven polypropylene reduces the extent of biofouling coverage of the material measured after 7 days of immersion, Fig. 8. This may be due to bubbles increasing the dissolved gas content in the water surrounding the material and extending entrapped gas layer lifetimes but not sufficiently to prevent fouling completely [91]. Biofouling is almost completely inhibited for CF$_4$ plasma treated nonwoven polypropylene with continuous air bubble release (flowrate = 1200 cm^3 min^{-1}). Colourimetry measurements confirm that CF$_4$ plasma treated textile samples continuously exposed to air bubbles are fouled to a lesser degree (have a smaller overall colour change) than all other samples, Supplementary Material Fig. S13. A good correlation is also found between the red–green colour change (Δa^*) and the blue–yellow colour change (Δb^*). This suggests that similar organisms are responsible for the biofouling of all immersed samples and the level of fouling directly correlates to the surface colour change. The levels of fouling (colour change) measured on untreated nonwoven polypropylene is also dramatically reduced through the addition of air bubbles. Through a combination of optical imaging and colourmetric analysis it has been demonstrated that maintaining an entrapped air cushion for superhydrophobic and aerophilic porous materials prevents biofouling.

4. Discussion

Feathers belonging to waterfowl and seabirds have remarkable water repellency [7]. This characteristic is attributable to a combination of their hierarchical fibrillar microstructure and hydrophobic preen oil coating leading to the Cassie–Baxter hydrophobicity effect [92]. In the current study, the angles measured between the mallard feather central rachis and barbs (41.6 ± 4.9°), between the barbs and barbules (43.0 ± 3.2°), and between barbules and hooklets (39.2 ± 5.9°) are comparable to the hierarchical structure of *Thuja plicata* tree branchlets—which display exceptional water channelling properties [93], Fig. 1 and Fig. 3. This finding implies that mallard feathers are not only water repellent but have also evolved to resist water ingress via water channelling away from the body.

The liquid repellent performance of the mallard feather has been mimicked using a nonwoven polypropylene textile with fibre diameters (3.4 ± 1.9 μm) of comparable length scale to the mallard feather barbules (8.4 ± 1.5 μm), Fig. 6. In order to replicate the mallard's hydrophobic preen oil, the nonwoven polypropylene textile was CF$_4$ plasma functionalised. Carbon–hydrogen bond substitution by electrical discharge reactive fluorine atoms to form carbon–fluorine bonds (fluorination) is the dominant chemical reaction pathway during CF$_4$ plasma treatment of saturated hydrocarbon polymer substrate surfaces [81]. These highly electronegative fluorinated carbon groups on the nonwoven polypropylene fibre surfaces lower the surface energy due to weakened liquid–solid intermolecular forces [94]. This combination of micro-fibrous surface roughness and low surface energy culminates in enhanced hydrophobicity and aerophilicity of the nonwoven polypropylene textile [58,95]. Structural and chemical analysis using SEM and XPS techniques respectively have shown that the rise in static water contact angle values (as well as the fall in water contact angle hysteresis and sliding angle values) following CF$_4$ plasma treatment of nonwoven polypropylene stems predominantly from surface fluorination (given that there is no marked change in surface topography), Fig. 3.

Trapping larger volumes of gas underwater by the aerophilic CF$_4$ plasma treated nonwoven polypropylene textile provides more gas for spreading at the textile surface–liquid interface, Fig. 4. The lower weight samples sustained trapped air layers for longer periods, despite the identical surface chemistry, similar BET specific surface area, and indistinguishable micro-fibre structure of the low (20 g m^{-2} grade) and high (35 g m^{-2} grade) weight nonwoven polypropylene textiles, Table 1. This is likely to be due to the greater bulk porosity of the 20 g m^{-2} grade material (0.91 ± 0.01) compared with the 35 g m^{-2} grade material (0.88 ± 0.01) given that the less tightly bound textile fibres allow a greater volume of gas to be trapped at the surface [1], provide better internal gas transport properties [96], and may improve air layer stability through the pneumatic spring effect [97]. The combination of textile bulk and surface properties for retaining entrapped air layers suggests that an air cushion with gas throughout the entire porous structure is beneficial for prolonged period trapped gas layer retention. Evidence for air cushion formation is provided by the release of air bubbles (< 1 s bursts, total volume = 1.9 ± 0.8 mL) below samples placed in the entrapped gas layer apparatus, Fig. 6. Upwards bulging of the test sample middle during bubble release from below can be taken as indicative of the internal air cushion collapse due to liquid ingress into the pores blocking upwards gas transportation through the material [86, 89]. Although the mallard feather structure is more ordered than the

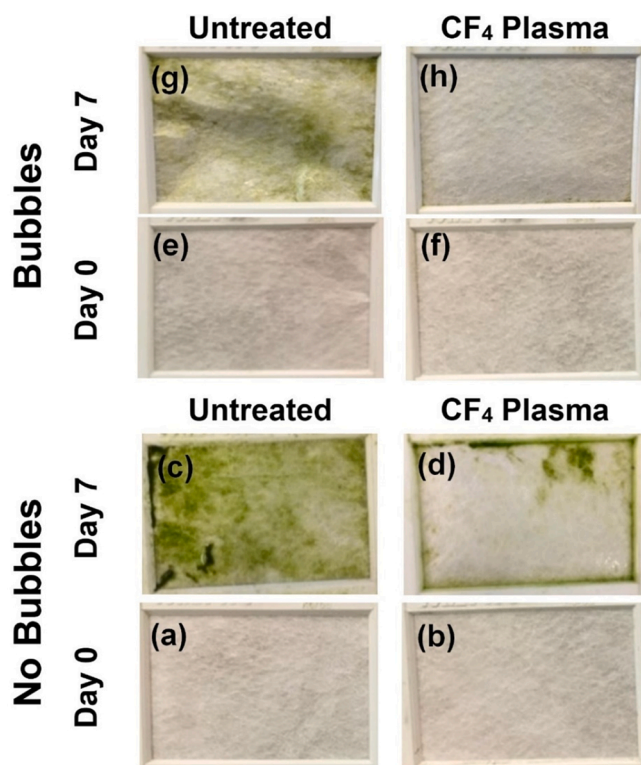**Fig. 8.** Pond water biofouling under accelerated conditions for untreated and CF$_4$ plasma treated (30 W) nonwoven polypropylene (20 g m^{-2}): samples (a–d) not exposed to bubbles; and samples (e–h) continuous stream of air bubbles (flowrate = 1200 cm^3 min^{-1}, with excess bubbles released through holes in the sample-mount-box).

random structure of the nonwoven textile, it has been shown that the mallard feather and CF_4 plasma functionalised nonwoven polypropylene display comparable bubble formation behaviours, Fig. 6. Therefore, the mallard feather has served as a good source of nature-inspired anti-biofouling materials design.

Trapped gas layers at solid–liquid interfaces are sought for applications such as drag reduction, where the air layer acts as a lubricant to reduce friction between the immersed object surface and the surrounding water [44,98,99]. They can also act as a physical barrier against harmful chemicals and organisms responsible for biofouling [50, 100]. Biofouling (the settlement and growth of microscopic and macroscopic organisms on submerged surfaces) causes a range of problems for the maritime industries, including hydrodynamic penalties which increase fuel consumption of vessels [101], accelerated deterioration of surfaces through microbially-induced corrosion [102], increased drag and loading on static structures [103], and facilitating spread of invasive species across the globe [104]. Developing eco-friendly methods to prevent such biofouling has been a long-standing challenge that necessitates broad-spectrum activity against the large taxonomic diversity of biofouling organisms (of which over 4000 species have been recorded to date [105]). Achieving such broad-spectrum activity without causing collateral harm to the environment has proven elusive via conventional chemical strategies [106, 107]. One physicochemical approach is to produce materials with complex surface microstructures that can passively reduce surface biofouling through foul release effects [108], the rupturing cell walls of settling organisms [109], or by minimising adhesion strength by limiting attachment sites [110,111]. Such micro/nanostructures with low surface energies provide an additional antibiofouling effect through the trapping of air within the structures to form a barrier preventing interactions between biological material and the solid surface to inhibit settlement [112–114]. Therefore the utilisation of surfaces that entrap air layers as a physical barrier to prevent the attachment of fouling organisms is a promising approach given its inherently broad-spectrum efficacy and lack of harm to the environment [50,115]. Such solid–liquid interface trapped air layers found on natural superhydrophobic plant leaf surfaces last around 2 days [116]. Longer lasting interfacial gas layers are reported for the elytra of aquatic insects such as the Common Backswimmer (*Notonecta glauca*) and the Saucer Bug (*Ilyocoris cimicoides*)—due to the high density of small hairs (microtrichia) [117]. Their stability is dependent upon several factors including liquid pressure, liquid surface tension, dissolved gas saturation, surface chemistry, and surface microstructure [91,118–120]. Eventually, the gas layers are lost through dissolution into surrounding water [41,43]. Manmade replication of such trapped air layers suffers from the coatings requiring complex fabrication procedures under harsh conditions and mechanical fragility [29,121]. In order to address these drawbacks, inspiration has been drawn from the behaviour of the diving bell spider [52,53]. It has been shown that entrapped gas layers can be sustained over a prolonged time (29 days) by passing solar powered air bubbles through a porous superhydrophobic and aerophilic material (CF_4 plasma treated nonwoven polypropylene), Fig. 7. This leads to the inhibition of biofouling under real-world outdoor conditions due to the gaseous layer physically separating the bulk fluid (which contains the fouling organisms and material) from the solid surface [41,50], Fig. 8. The bubbles also contribute a concurrent antifouling effect by disrupting the settlement of organisms responsible for biofouling [122]. When air bubbles are released below the less water repellent control material (untreated nonwoven polypropylene), liquid ingress of the bottom surface is triggered by pressure fluctuations due to bubbles which then blocks gas transport through the material. Collapse of the surface air layer causes wetting of the material leading to biofouling, Fig. 8 [89,90]. Alternative substrates for the formation of trapped air cushion surfaces could include superhydrophobic low contact angle hysteresis zinc oxide coated textiles, with scope for the photocatalytic inorganic coating to generate gas from water in situ for the trapped layer [123].

The described approach holds significant potential for long-term real-world applications. Establishing and maintaining solid–liquid interface trapped gas layers on submerged marine structures presents an inherently taxonomically-independent physical barrier against biofouling [50,100] and non-biological corrosion [124,125]. Scale-up can draw upon bubble delivery systems for large surface areas in the marine environment [122,126] in combination with established industrial scale production of plasma functionalised textiles [127]. For example, marine structures (harbour pontoons etc.) can be encased with plastron forming functional textiles and connected to a supply of air bubbles. Moreover, because air layers are lubricous and reduce friction between immersed surfaces and the surrounding water (drag reduction [44,98,99]), the methodology could be used to increase the speed of high-performance watercraft or reduce wall shear stress to improve flow rates within pipework.

5. Conclusions

The trapped surface air layer formed during immersion of mallard bird feathers into water has been replicated using low cost and scalable CF_4 plasmachemical functionalisation of nonwoven polypropylene textile—mimicking a combination of micro-fibrous surface roughness and low surface energy. A strong correlation has been observed between static water droplet contact angle, hydrostatic breakthrough pressure, and extent of solid–liquid interface gas layer entrapment (bubble diameters). Trapped gas layers last up to 4.8 days in static water immersion. Drawing bioinspiration from the diving bell spider, solar-powered pulsing (< 1 s bursts) of a gas bubble stream every 2 h into CF_4 plasma functionalised nonwoven polypropylene further extends the trapped gas layer lifetime to 29 days. This use of gas bubbles to maintain the trapped air layers on nonwoven polypropylene improves the antibiofouling performance in real-world outdoor conditions (pond water). The correlation between porosity and lifetime of trapped gas layer for the same surface chemistry confirms that there is gas cushion formation rather than a gas layer localised at just the substrate surface (solid–liquid interface). This combined nature-inspired approach holds significant potential for eco-friendly antibiofouling surfaces without collateral harm to the environment.

CRediT authorship contribution statement

J. P. S. B., J. M. R., P. C., and G. H. devised the bioinspired approach for trapped gas layer surfaces. J. M. R. undertook plasmachemical surface functionalisation, contact angle analysis, hydrostatic breakthrough pressure measurements, solid–liquid interface trapped gas layer, and biofouling experiments. H. J. C. performed XPS analysis. J. P. S. B. and J. M. R. jointly drafted the manuscript. All authors have given final approval for publication.

Declaration of Competing Interest

Cawthron Institute and Durham University have filed a joint international patent application.

Data Availability

Data created during this research can be accessed at https://collections.durham.ac.uk.

Acknowledgements

Appendix A. Supporting information

Supplementary data associated with this article can be found in the online version at doi:10.1016/j.colsurfa.2022.130491.

References

[1] A.M. Rijke, Feather structure and behavioral patterns in seabirds. *In Seabirds*, IntechOpen, 2018, pp. 7–25.

[2] R.S. Seymour, P.G.D. Matthews, Physical gills in diving insects and spiders: theory and experiment, J. Exp. Biol. 216 (2013) 164–170.

[3] S. Baxter, A.B.D. Cassie, 8—the water repellency of fabrics and a new water repellency test, J. Text. Inst. Trans. 36 (1945) T67–T90.

[4] M. Giraudeau, C. Duval, N. Guillon, V. Bretagnolle, C. Gutierrez, P. Heeb, Effects of access to preen gland secretions on mallard plumage, Naturwissenschaften 97 (2010) 577–581.

[5] S. Srinivasan, S.S. Chhatre, J.O. Guardado, K.C. Park, A.R. Parker, M.F. Rubner, G.H. McKinley, R.E. Cohen, Quantification of feather structure, wettability and resistance to liquid penetration, J. R. Soc. Interface 11 (2014), 1120140287.

[6] A.B.D. Cassie, S. Baxter, Large contact angles of plant and animal surfaces, Nature 155 (1945) 21–22.

[7] R. Stephenson, C.A. Andrews, The effect of water surface tension on feather wettability in aquatic birds, Can. J. Zool. 75 (1997) 288–294.

[8] G. Lambert, D.B. Peakall, B.J.R. Philogène, F.R. Engelhardt, Effect of oil and oil dispersant mixtures on the basal metabolic rate of ducks, Bull. Environ. Contam. Toxicol. 29 (1982) 520–524.

[9] C.E. Korschgen, K.P. Kenow, W.L. Green, D.H. Johnson, M.D. Samuel, L. Sileo, Survival of radiomarked canvasback ducklings in northwestern minnesota, J. Wildl. Manag. 60 (1996) 120.

[10] M.R. Banta, A.J. Lynott, M.J. VanSant, G.S. Bakken, Partitioning heat loss from mallard ducklings swimming on the air-water interface, J. Exp. Biol. 207 (2004) 4551–4557.

[11] V.M. Mendenhall, H. Milne, Factors affecting duckling survival of eiders *Somateria mollissima* in northeast scotland, Ibis (Lond. 1859 *127*) (1985) 148–158.

[12] A.B.D. Cassie, S. Baxter, Wettability of porous surfaces, Trans. Faraday Soc. 40 (1944) 546–551.

[13] E. Bormashenko, Y. Bormashenko, T. Stein, G. Whyman, E. Bormashenko, Why do pigeon feathers repel water? Hydrophobicity of pennae, cassie-baxter wetting hypothesis and cassie-wenzel capillarity-induced wetting transition, J. Colloid Interface Sci. 311 (2007) 212–216.

[14] E. Bormashenko, O. Gendelman, G. Whyman, Superhydrophobicity of lotus leaves versus birds wings: different physical mechanisms leading to similar phenomena, Langmuir 28 (2012) 14992–14997.

[15] A. Kovalev, A.E. Filippov, S.N. Gorb, Unzipping bird feathers, J. R. Soc. Interface 11 (2014) 20130988.

[16] A.M. Rijke, S.W. Evans, H. Bouwman, Water repellency and feather structure of the blue swallow *Hirundo atrocaerulea*, Ostrich 71 (2000) 143–145.

[17] H.A. Soini, D.J. Whittaker, D. Wiesler, E.D. Ketterson, M.V. Novotny, Chemosignaling diversity in songbirds: chromatographic profiling of preen oil volatiles in different species, J. Chromatogr. A 1317 (2013) 186–192.

[18] E.M. Levy, P.M. Strain, The composition of the preen gland waxes of some marine birds: a word of caution for chemotaxonomists, Comp. Biochem. Physiol. – Part B Biochem. 72 (2) (1982) 255–260.

[19] Z. Wang, Z. Guo, Biomimetic superwettable materials with structural colours, Chem. Commun. 53 (2017) 12990–13011.

[20] H. Wu, R. Zhang, Y. Sun, D. Lin, Z. Sun, W. Pan, P. Downs, Biomimetic nanofiber patterns with controlled wettability, Soft Matter 4 (2008) 2429–2433.

[21] S. Wang, Z. Yang, G. Gong, J. Wang, J. Wu, S. Yang, L. Jiang, Icephobicity of penguins *Spheniscus humboldti* and an artificial replica of penguin feather with air-infused hierarchical rough structures, J. Phys. Chem. C 120 (2016) 15923–15929.

[22] Y. Liu, X. Chen, J.H. Xin, Hydrophobic duck feathers and their simulation on textile substrates for water repellent treatment, Bioinspiration Biomim. 3 (2008), 046007.

[23] K. Luan, M. He, B. Xu, P. Wang, J. Zhou, B. Hu, L. Jiang, H. Liu, Spontaneous directional self-cleaning on the feathers of the aquatic bird *Anser cygnoides domesticus* induced by a transient superhydrophilicity, Adv. Funct. Mater. 31 (2021) 2010634.

[24] S.F. Ahmadi, V. Umashankar, Z. Dean, B. Chang, S. Jung, J.B. Boreyko, How multilayered feathers enhance underwater superhydrophobicity, ACS Appl. Mater. Interfaces 13 (2021) 27567–27574.

[25] T. Khudiyev, T. Dogan, M. Bayindir, Biomimicry of multifunctional nanostructures in the neck feathers of mallard (*Anas platyrhynchos* L.) Drakes, Sci. Rep. 4 (2014) 1–6.

[26] S. Atherton, J.C. Brennan, R.H. Morris, J.D.E. Smith, C.A.E. Hamlett, G. McHale, N.J. Shirtcliffe, M.I. Newton, Plastron respiration using commercial fabrics, Materials 7 (2014) 484.

[27] C.H. Choi, Y. Kwak, M.K. Kim, D.G. Kim, Effective harmful organism management i: fabrication of facile and robust superhydrophobic coating on fabric, Sustain 12 (2020) 5876.

[28] Y. Zheng, X. Zhou, Z. Xing, T. Tu, Exploring the underwater air-retaining ability and thermal insulating effect of terry fabrics inspired by *Salvinia molesta*, Text. Res. J. 89 (2019) 2859–2869.

[29] J. Zimmermann, F.A. Reifler, G. Fortunato, L.C. Gerhardt, S. Seeger, A simple, one-step approach to durable and robust superhydrophobic textiles, Adv. Funct. Mater. 18 (2008) 3662–3669.

[30] D.M. Warsinger, A. Servi, S. Van Belleghem, J. Gonzalez, J. Swaminathan, J. Kharraz, H.W. Chung, H.A. Arafat, K.K. Gleason, J.H. Lienhard V, Combining air recharging and membrane superhydrophobicity for fouling prevention in membrane distillation, J. Memb. Sci. 505 (2016) 241–252.

[31] G.B. Hwang, K. Page, A. Patir, S.P. Nair, E. Allan, I.P. Parkin, The anti-biofouling properties of superhydrophobic surfaces are short-lived, ACS Nano 12 (2018) 6050–6058.

[32] E.M. Domingues, S. Arunachalam, J. Nauruzbayeva, H. Mishra, Biomimetic coating-free surfaces for long-term entrapment of air under wetting liquids, Nat. Commun. 9 (2018) 1–11.

[33] J. Wang, S. Lee, A.R. Bielinski, K.A. Meyer, A. Dhyani, A.M. Ortiz-Ortiz, A. Tuteja, N.P. Dasgupta, Rational design of transparent nanowire architectures with tunable geometries for preventing marine fouling, Adv. Mater. Interfaces 7 (2020) 2000672.

[34] F. Hizal, N. Rungraeng, J. Lee, S. Jun, H.J. Busscher, H.C. Van Der Mei, C.H. Choi, Nanoengineered superhydrophobic surfaces of aluminum with extremely low bacterial adhesivity, ACS Appl. Mater. Interfaces 9 (2017) 12118–12129.

[35] J. Ma, Y. Sun, K. Gleichauf, J. Lou, Q. Li, Nanostructure on taro leaves resists fouling by colloids and bacteria under submerged conditions, Langmuir 27 (2011) 10035–10040.

[36] H. Hu, J. Wen, L. Bao, L. Jia, D. Song, B. Song, G. Pan, M. Scaraggi, D. Dini, Q. Xue, F. Zhou, Significant and stable drag reduction with air rings confined by alternated superhydrophobic and hydrophilic strips, Sci. Adv. 3 (2017), e1603288.

[37] R. Poetes, K. Holtzmann, K. Franze, U. Steiner, Metastable underwater superhydrophobicity, Phys. Rev. Lett. 105 (2010) 166104.

[38] J. Seo, R. García-Mayoral, A. Mani, Turbulent flows over superhydrophobic surfaces: flow-induced capillary waves, and robustness of air-water interfaces, J. Fluid Mech. 835 (2018) 45–85.

[39] P.R. Jones, X. Hao, E.R. Cruz-Chu, K. Rykaczewski, K. Nandy, T.M. Schutzius, K. K. Varanasi, C.M. Megaridis, J.H. Walther, P. Koumoutsakos, H.D. Espinosa, N. A. Patankar, Sustaining dry surfaces under water, Sci. Rep. 5 (2015) 12311.

[40] Y. Xiang, S. Huang, T.Y. Huang, A. Dong, D. Cao, H. Li, Y. Xue, P. Lv, H. Duan, Superrepellency of underwater hierarchical structures on salvinia leaf, Proc. Natl. Acad. Sci. U. S. A. 117 (2020) 2282–2287.

[41] T. Simovich, A. Rosenhahn, R.N. Lamb, Thermoregeneration of plastrons on superhydrophobic coatings for sustained antifouling properties, Adv. Eng. Mater. 22 (2020) 1900806.

[42] C. Thamaraiselvan, E. Manderfeld, M.N. Kleinberg, A. Rosenhahn, C.J. Arnusch, Superhydrophobic candle soot as a low fouling stable coating on water treatment membrane feed spacers, ACS Appl. Bio Mater. 4 (2021) 4191–4200.

[43] M. Xu, C.T. Liu, C.J. Kim, Self-powered plastron preservation and one-step molding of semiactive superhydrophobic surfaces, Langmuir 36 (2020) 8193–8198.

[44] P. Du, J. Wen, Z. Zhang, D. Song, A. Ouahsine, H. Hu, Maintenance of air layer and drag reduction on superhydrophobic surface, Ocean Eng. 130 (2017) 328–335.

[45] J. Marlena, J.K.S. Tan, Z. Lin, D.X. Li, B. Zhao, H.L. Leo, S. Kim, C.H. Yap, Monolithic polymeric porous superhydrophobic material with pneumatic plastron stabilization for functionally durable drag reduction in blood-contacting biomedical applications, NPG Asia Mater. 13 (2021) 1–12.

[46] Z. Li, J. Marlena, D. Pranantyo, B.L. Nguyen, C.H. Yap, A porous superhydrophobic surface with active air plastron control for drag reduction and fluid impalement resistance, J. Mater. Chem. A 7 (2019) 16387–16396.

[47] F. Vüllers, Y. Germain, L.M. Petit, H. Hölscher, M.N. Kavalenka, Pressure-stable air-retaining nanostructured surfaces inspired by natural air plastrons, Adv. Mater. Interfaces 5 (2018) 1800125.

[48] Schimmel, T. Gas-Containing Surface Cover, Arrangement, and Use. Patent US20200216424, 2020.

[49] Schimmel, T. Structured Gas Containing Surfaces. Patent US2021033119A1, 2020.

[50] J. Arnott, A.H.F. Wu, M.J. Vucko, R.N. Lamb, Marine antifouling from thin air, Biofouling 30 (2014) 1045–1054.

[51] J.H. Thorp, D.C. Rogers, W.W. Dimmick, Thorp and Covich's Freshwater Invertebrates: Ecology and General Biology, Vol. 1, Elsevier,, 2014.

[52] R.S. Seymour, S.K. Hetz, The diving bell and the spider: the physical gill of *Argyroneta aquatica*, J. Exp. Biol. 214 (2011) 2175–2181.

[53] D. Neumann, D. Woermann, Stability of the volume of air trapped on the abdomen of the water spider *Argyroneta aquatica*, SpringerPlus 2 (2013) 694.

[54] Y. Ning, D. Zhang, S. Ben, Z. Zhao, J. Zha, D. Tian, K. Liu, L. Jiang, An innovative design by single-layer superaerophobic mesh: continuous underwater bubble antibuoyancy collection and transportation, Adv. Funct. Mater. 30 (2020) 1907027.

[55] J. Huo, J. Yong, F. Chen, Q. Yang, Y. Fang, X. Hou, Trapped air-induced reversible transition between underwater superaerophilicity and superaerophobicity on the femtosecond laser-ablated superhydrophobic PTFE surfaces, Adv. Mater. Interfaces 6 (2019) 1900262.

[56] J. Yong, F. Chen, J. Huo, Y. Fang, Q. Yang, J. Zhang, X. Hou, Femtosecond laser induced underwater superaerophilic and superaerophobic PDMS sheets with through microholes for selective passage of air bubbles and further collection of underwater gas, Nanoscale 10 (2018) 3688–3696.

[57] J. Yong, F. Chen, Y. Fang, J. Huo, Q. Yang, J. Zhang, H. Bian, X. Hou, Bioinspired design of underwater superaerophobic and superaerophilic surfaces by femtosecond laser ablation for anti- or capturing bubbles, ACS Appl. Mater. Interfaces 9 (2017) 39863–39871.

[58] L. Rapoport, T. Emmerich, K.K. Varanasi, Capturing bubbles and preventing foam using aerophilic surfaces, Adv. Mater. Interfaces 7 (2020) 1901599.

[59] A.M. Hynes, M.J. Shenton, J.P.S. Badyal, Pulsed plasma polymerization of perfluorocyclohexane, Macromolecules 29 (1996) 4220–4225.

[60] C.D. Ehrlich, J.A. Basford, Recommended practices for the calibration and use of leaks, J. Vac. Sci. Technol. A Vac., Surf., Film. 10 (1992) 1–17.

[61] R. Strapasson, S.C. Amico, M.F.R. Pereira, T.H.D. Sydenstricker, Tensile and impact behavior of polypropylene/low density polyethylene blends, Polym. Test. 24 (2005) 468–473.

[62] R.T. Ogulata, S. Mavruz, Investigation of porosity and air permeability values of plain knitted fabrics, Fibres Text. East. Eur. 82 (2010) 71–75.

[63] R.M. Friedman, J. Hudis, M.L. Perlman, Chemical effects on linewidths observed in photoelectron spectroscopy, Phys. Rev. Lett. 29 (1972) 692.

[64] R.H. Dettre, R.E. Johnson, Contact Angle Hysteresis. Contact Angle, Wettability, Adhes, 1964, pp. 136–144.

[65] A.F. Stadler, G. Kulik, D. Dage, L. Barbieri, P. Hoffmann, A Snake-Based Approach to Accurate Determination of Both Contact Points and Contact Angles, Colloids Surf. A Physicochem. Eng. Asp. 286 (2006) 92–103.

[66] C.C. Chang, C.J. Wu, Y.J. Sheng, H.K. Tsao, Anti-smudge behavior of facilely fabricated liquid-infused surfaces with extremely low contact angle hysteresis property, RSC Adv. 6 (2016) 19214–19222.

[67] K.R. Lamison, A.J. Guenthner, J.M. Mabry, Water breakthrough pressure of cotton fabrics treated with fluorinated silsesquioxane/fluoroelastomer coatings, Appl. Surf. Sci. 258 (2012) 10205–10208.

[68] B.P. Saville, Comfort. In Physical Testing of Textiles, Elsevier, 1999, pp. 209–243.

[69] H. Rathgen, F. Mugele, Microscopic shape and contact angle measurement at a superhydrophobic surface, Faraday Discuss. 146 (2010) 49–56.

[70] J.Y. Park, J. Ryu, S.J. Lee, Penetration of a bubble through porous membranes with different wettabilities, Soft Matter 15 (2019) 5819–5826.

[71] A.B. Şengül, M.M. Rahman, E. Asmatulu, Evaluation of media and light source effects on the growth of botryococcus braunii for biofuel production, Int. J. Environ. Sci. Technol. 16 (2019) 3193–3202.

[72] B. Pitts, M.A. Hamilton, G.A. McFeters, P.S. Stewart, A. Willse, N. Zelver, Color measurement as a means of quantifying surface biofouling, J. Microbiol. Methods 34 (1998) 143–149.

[73] E. Quagliarini, A. Gianangeli, M. D'Orazio, B. Gregorini, A. Osimani, L. Aquilanti, F. Clementi, Effect of temperature and relative humidity on algae biofouling on different fired brick surfaces, Constr. Build. Mater. 199 (2019) 396–405.

[74] B. Hill, T. Roger, F.W. Vorragen, Comparative analysis of the quantization of color spaces on the basis of the CIELAB color-difference formula, ACM Trans. Graph. 16 (1997) 109–154.

[75] A.M. Rijke, The water repellency and feather structure of cormorants, phalacrocoracidae, J. Exp. Biol. 48 (1968) 185–189.

[76] A. Elowson, Spread-wing postures and the water repellency of feathers: a test of rijke's hypothesis, Auk 101 (1984) 371–383.

[77] J. Hopkins, R.D. Boyd, J.P.S. Badyal, Plasma fluorination versus oxygenation of polypropylene, J. Phys. Chem. 100 (1996) 6755–6759.

[78] N.D. Yilmaz, P. Banks-Lee, N.B. Powell, S. Michielsen, Effects of porosity, fiber size, and layering sequence on sound absorption performance of needle-punched nonwovens, J. Appl. Polym. Sci. 121 (5) (2011) 3056–3069.

[79] H.H. Epps, K.K. Leonas, Pore size and air permeability of four nonwoven fabrics, Int. Nonwovens J. 9 (2) (2000) 18–22.

[80] M. Thommes, K. Kaneko, A.V. Neimark, J.P. Olivier, F. Rodriguez-Reinoso, J. Rouquerol, K.S.W. Sing, Physisorption of gases, with special reference to the evaluation of surface area and pore size distribution (IUPAC Technical Report), Pure Appl. Chem. 87 (9–10) (2015) 1051–1069.

[81] J. Hopkins, J.P.S. Badyal, Nonequilibrium glow discharge fluorination of polymer surfaces, J. Phys. Chem. 99 (1995) 4261–4264.

[82] 3 M Innovative Properties Co. Method of Making Fluorinated Electrets. *Patent* US20030177908A1, March 18, 2003.

[83] A.Plasma Grill, Assisted Etching, *Cold Plasma Mater. Fabr.*; IEEE (1994) 216–245.

[84] W.C.E. Schofield, J.P.S. Badyal, Plasmachemical oxygenation of porous polymer surfaces for stable hydrophilicity and enhanced liquid absorption, Polymer 52 (2011) 5732–5738.

[85] D. Panchanathan, A. Rajappan, K.K. Varanasi, G.H. McKinley, Plastron regeneration on submerged superhydrophobic surfaces using in situ gas generation by chemical reaction, ACS Appl. Mater. Interfaces 10 (2018) 33684–33692.

[86] J. Chen, Y. Liu, D. Guo, M. Cao, L. Jiang, Under-water unidirectional air penetration via a janus mesh, Chem. Commun. 51 (2015) 11872–11875.

[87] C. Shi, X. Cui, X. Zhang, P. Tchoukov, Q. Liu, N. Encinas, M. Paven, F. Geyer, D. Vollmer, Z. Xu, H.J. Butt, H. Zeng, Interaction between Air Bubbles and Superhydrophobic surfaces in aqueous solutions, Langmuir 31 (2015) 7317–7327.

[88] J. Zhang, X. Sheng, L. Jiang, The dewetting properties of lotus leaves, Langmuir 25 (2009) 1371–1376.

[89] J. Huo, Q. Yang, J. Yong, P. Fan, Y. Lu, Feng, X. Hou, F. Chen, Underwater Superaerophobicity/Superaerophilicity and Unidirectional Bubble Passage Based on the Femtosecond Laser-Structured Stainless Steel Mesh, Adv. Mater. Interfaces 7 (2020) 1902128.

[90] C. Chen, L.A. Shi, Z. Huang, Y. Hu, S. Wu, J. Li, D. Wu, J. Chu, Microhole-arrayed PDMS with controllable wettability gradient by one-step femtosecond laser drilling for ultrafast underwater bubble unidirectional self-transport, Adv. Mater. Interfaces 6 (2019) 1900297.

[91] Y. Xiang, S. Huang, P. Lv, Y. Xue, Q. Su, H. Duan, Ultimate stable underwater superhydrophobic state, Phys. Rev. Lett. 119 (2017), 134501.

[92] A.M. Rijke, Wettability and phylogenetic development of feather structure in water birds, J. Exp. Biol. 52 (1970) 469–479.

[93] R.M. Von Spreckelsen, M.T. Harris, J.M. Wigzell, R.C. Fraser, A. Carletto, D.P. K. Mosquin, D. Justice, J.P.S. Badyal, Bioinspired breathable architecture for water harvesting, Sci. Rep. 5 (2015) 16798.

[94] I. Woodward, W.C.E. Schofield, V. Roucoules, J.P.S. Badyal, Super-hydrophobic surfaces produced by plasma fluorination of polybutadiene films, Langmuir 19 (2003) 3432–3438.

[95] M.H. Shim, J. Kim, C.H. Park, The effects of surface energy and roughness on the hydrophobicity of woven fabrics, Text. Res. J. 84 (2014) 1268–1278.

[96] A.C. Goodings, Air flow through textile fabrics, Text. Res. J. 34 (1964) 713–724.

[97] D. Gandyra, S. Walheim, S. Gorb, P. Ditsche, W. Barthlott, T. Schimmel, Air retention under water by the floating fern salvinia: the crucial role of a trapped air layer as a pneumatic spring, Small 16 (2020) 2003425.

[98] R.J. Daniello, N.E. Waterhouse, J.P. Rothstein, Drag reduction in turbulent flows over superhydrophobic surfaces, Phys. Fluids 21 (2009), 085103.

[99] E. Aljallis, M.A. Sarshar, R. Datla, V. Sikka, A. Jones, C.H. Choi, Experimental study of skin friction drag reduction on superhydrophobic flat plates in high reynolds number boundary layer flow, Phys. Fluids 25 (2013), 025103.

[100] A.H.F. Wu, K. Nakanishi, K.L. Cho, R. Lamb, Diatom attachment inhibition: limiting surface accessibility through air entrapment, Biointerphases 8 (2013) 1–10.

[101] A. Farkas, S. Song, N. Degiuli, I. Martić, Y.K. Demirel, Impact of biofilm on the ship propulsion characteristics and the speed reduction, Ocean Eng. 199 (2020), 107033.

[102] V. Vishwakarma, K.G. Saravanan, Biofouling and Biocorrosion, *Polymetallic Coat. Control Biofouling Pipelines* (2021) 1–13.

[103] M. Apolinario, R. Coutinho, Understanding the Biofouling of Offshore and Deep-Sea Structures. In *Advances in Marine Antifouling Coatings and Technologies*, Woodhead Publishing,, 2009, pp. 132–147.

[104] I. Davidson, C. Scianni, C. Hewitt, R. Everett, E. Holm, M. Tamburri, G. Ruiz, Mini-Review: Assessing the Drivers of Ship Biofouling Management – Aligning Industry and Biosecurity Goals, Biofouling 32 (2016) 411–428.

[105] D.M. Yebra, S. Kiil, K. Dam-Johansen, Antifouling technology - past, present and future steps towards efficient and environmentally friendly antifouling coatings, Prog. Org. Coat. 50 (2004) 75–104.

[106] S. Nir, M. Reches, Bio-Inspired antifouling approaches: the quest towards non-toxic and non-biocidal materials, Curr. Opin. Biotechnol. 39 (2016) 48–55.

[107] G. Jones, The Battle against Marine Biofouling: A Historical Review. In Advances in Marine Antifouling Coatings and Technologies, Woodhead Publishing,, 2009, pp. 19–45.

[108] A.M. Brzozowska, F.J. Parra-Velandia, R. Quintana, Z. Xiaoying, S.S.C. Lee, L. Chin-Sing, D. Jańczewski, S.L.M. Teo, J.G. Vancso, Biomimicking micropatterned surfaces and their effect on marine biofouling, Langmuir 30 (30) (2014) 9165–9175.

[109] G.S. Watson, D.W. Green, J.A. Watson, Z. Zhou, X. Li, G.S.P. Cheung, M. Gellender, A simple model for binding and rupture of bacterial cells on nanopillar surfaces, Adv. Mater. Interfaces 6 (10) (2019) 1801646.

[110] A.E. Vellwock, H. Yao, Biomimetic and bioinspired surface topographies as a green strategy for combating biofouling: a review, Bioinspiration Biomim. 16 (4) (2021) 041003.

[111] K.D. Esmeryan, I.A. Avramova, C.E. Castano, I.A. Ivanova, R. Mohammadi, E. I. Radeva, D.S. Stoyanova, T.G. Vladkova, Early stage anti-bioadhesion behavior of superhydrophobic soot based coatings towards *Pseudomonas putida*, Mater. Des. 160 (2018) 395–404.

[112] K.D. Esmeryan, C.E. Castano, T.A. Chaushev, R. Mohammadi, T.G. Vladkova, Silver-doped superhydrophobic carbon soot coatings with enhanced wear resistance and anti-microbial performance, Colloids Surf. A Physicochem. Eng. Asp. 582 (2019), 123880.

[113] J. Bruzaud, J. Tarrade, E. Celia, T. Darmanin, E. Taffin de Givenchy, F. Guittard, J.M. Herry, M. Guilbaud, M.N. Bellon-Fontaine, The design of superhydrophobic stainless steel surfaces by controlling nanostructures: a key parameter to reduce the implantation of pathogenic bacteria, Mater. Sci. Eng. C. 73 (2017) 40–47.

[114] S.H. Yoon, N. Rungraeng, W. Song, S. Jun, Superhydrophobic and superhydrophilic nanocomposite coatings for preventing *Escherichia coli* K-12 adhesion on food contact surface, J. Food Eng. 131 (2014) 135–141.

[115] Y. Cai, W. Bing, C. Chen, Z. Chen, Gaseous plastron on natural and biomimetic surfaces for resisting marine biofouling, Molecules 26 (2021) 2592.

[116] Z. Cerman, B.F. Striffler, W. Barthlott, Dry in the Water: The Superhydrophobic Water Fern Salvinia - A Model for Biomimetic Surfaces, in: *Functional Surfaces in Biology*, Springer, Netherlands, 2009, pp. 97–111.

[117] A. Balmert, H. Florian Bohn, P. Ditsche-Kuru, W. Barthlott, Dry under water: comparative morphology and functional aspects of air-retaining insect surfaces, J. Morphol. 272 (2011) 442–451.

[118] M.A. Samaha, H. Vahedi Tafreshi, M. Gad-el-Hak, Sustainability of superhydrophobicity under pressure, Phys. Fluids 24 (2012), 112103.

[119] M.S. Bobji, S.V. Kumar, A. Asthana, R.N. Govardhan, Underwater sustainability of the "*cassie*" state of wetting, Langmuir 25 (2009) 12120–12126.

[120] M. Sakai, T. Yanagisawa, A. Nakajima, Y. Kameshima, K. Okada, Effect of surface structure on the sustainability of an air layer on superhydrophobic coatings in a water-ethanol mixture, Langmuir 25 (2009) 13–16.

[121] G.R.J. Artus, S. Seeger, One-dimensional silicone nanofilaments, Adv. Colloid Interface Sci. 209 (2014) 144–162.

[122] G.A. Hopkins, F. Gilbertson, O. Floerl, P. Casanovas, M. Pine, P. Cahill, Continuous bubble streams for controlling marine biofouling on static artificial structures, PeerJ 9 (2021), e11323.

[123] T.J. Wood, G.A. Hurst, W.C.E. Schofield, R.L. Thompson, G. Oswald, J.S.O. Evans, G.J. Sharples, C. Pearson, M.C. Petty, J.P.S. Badyal, Electroless deposition of multi-functional zinc oxide surfaces displaying photoconductive, superhydrophobic, photowetting, and antibacterial properties, J. Mater. Chem. 22 (2012) 3859–3867.

[124] T. Ishizaki, Y. Masuda, M. Sakamoto, Corrosion resistance and durability of superhydrophobic surface formed on magnesium alloy coated with nanostructured cerium oxide film and fluoroalkylsilane molecules in corrosive NaCl aqueous solution, Langmuir 27 (2011) 4780–4788.

[125] A.C.C. De Leon, R.B. Pernites, R.C. Advincula, Superhydrophobic colloidally textured polythiophene film as superior anticorrosion coating, ACS Appl. Mater. Interfaces 4 (2012) 3169–3176.

[126] A.J. Scardino, L.E. Fletcher, J.A. Lewis, Fouling control using air bubble curtains: protection for stationary vessels, Proc. Inst. Mar. Eng. Sci. Technol. Part A J. Mar. Eng. Technol. 8 (2009) 3–10.

[127] T.A. Miller, M.G. Mikhael, R. Ellwanger, A. Boufelfel, D. Booth, A. Yializis, Polymer multi-layer processing of thin film materials, MRS Proc. 555 (1999) 247–254.